INTERNATIONAL JOURNAL FOR NUMERICAL METHODS IN FLUIDS
Int. J. Numer. Meth. Fluids 2005; **48**:1041–1066
Published online 7 April 2005 in Wiley InterScience (www.interscience.wiley.com). DOI: 10.1002/fld.976

Flow simulation in the nip of a rigid forward roll coater

J. P. Mmbaga[1], R. E. Hayes[1,*,†], F. H. Bertrand[2] and P. A. Tanguy[2]

[1] *Department of Chemical and Material Engineering, University of Alberta, Edmonton, Alberta, Canada T6G 2G6*
[2] *URPEI, Department of Chemical Engineering, Ecole Polytechnique, Montréal, Québec, Canada H3T 1J7*

SUMMARY

This paper shows the development of an efficient solution algorithm for the simulation of a forward roll coating flows with free surfaces. The technique is based on the method of successive approximation combined with a method for rapidly finding a good starting point, i.e. a good initial computational domain. Movement of the free surface from the initial to final positions is demonstrated using both kinematic and normal stress schemes. Adaptive domain decomposition at each pseudo time step is performed with no significant cost penalty. The flow field is computed using a finite element solution of the Navier–Stokes equation.

The proposed scheme is shown to be flexible enough to accommodate different scenarios over the practical range of many applications, i.e. capillary numbers in the range of 0.01–300, and a wide range of gap settings and rotational speeds. A close match is found between simulation and experimental meniscus profiles as well as nip pressure profiles. Overall the technique is quite robust and is able to simulate a variety of coating flow situations without resorting to over-simplifications. Copyright © 2005 John Wiley & Sons, Ltd.

KEY WORDS: coating flow simulation; roll coating; mesh refinement; free surface algorithms; finite element method

1. INTRODUCTION

Film coating is a process in which a thin film of liquid is continuously deposited onto a moving substrate, which may subsequently be dried or cooled to produce a solid film. Film coating is widely used in the manufacture of, for example, printing paper, photographic film, magnetic tape and discs, adhesive tapes and labels. Coating processes include, for example, dip coating,

*Correspondence to: R. E. Hayes, Department of Chemical and Material Engineering, University of Alberta, Edmonton, Alberta, Canada T6G 2G6.
†E-mail: bob.hayes@ualberta.ca

Contract/grant sponsor: NSERC
Contract/grant sponsor: Paprican

Received 14 December 2004
Revised 15 February 2005
Accepted 21 February 2005

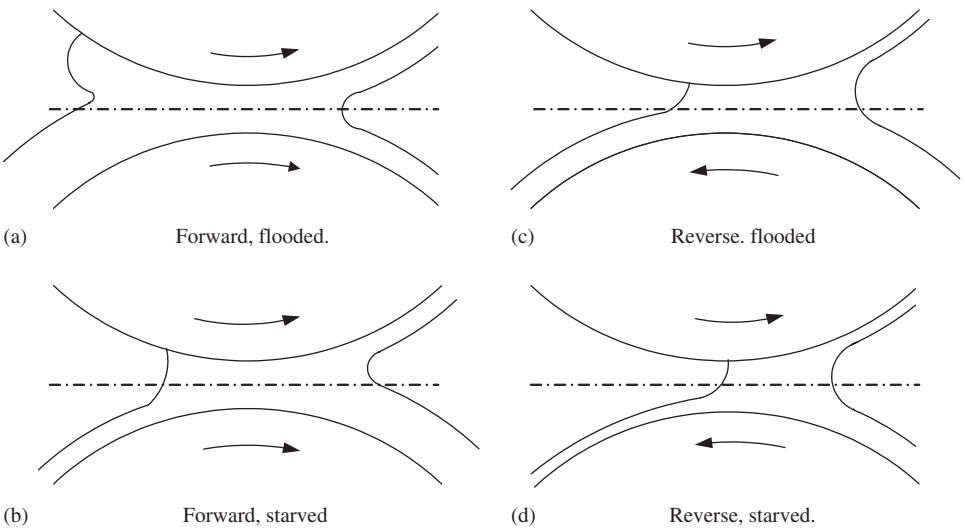

Figure 1. Roll coating configurations showing forward roll coating with (a) flooded nip; (b) starved nip and reverse roll coating with (c) flooded nip; and (d) starved nip.

slot coating, blade coating, slide-coating, curtain coating and roll coating. This work focuses on roll coating, in which pairs of rolls are used to metre and apply the liquid film. A pair of rolls can operate as either counter-rotating (forward roll coating) or co-rotating (reverse roll coating), as shown in Figure 1. They may operate in a flooded regime, see Figure 1(a) and (c), where the incoming film thickness exceeds the minimum clearance between the rolls, or in a starved regime where the thickness of the incoming film is either equal to or less than the minimum clearance, see Figure 1(b) and 1(d). Furthermore, the roll surfaces may be either rigid or covered with a deformable elastomer. Here, we consider the case of two counter-rotating rigid rolls.

The fluid mechanics of rigid roll coating have been investigated analytically [1–3], computationally [4–7] and experimentally [8–10]. Most work has been devoted to the flooded regime, including the measurement and prediction of pressure and velocity field distributions [2, 4, 5, 11–13], measurement and prediction of flux and film thickness [2, 3, 8], and the measurement of meniscus profiles [9, 10].

The main parameter used to characterize coating flows is the capillary number, which is the ratio of viscous and capillary forces. It is defined as

$$Ca = \frac{\mu U}{\sigma} \tag{1}$$

where U is the roll velocity, μ the fluid viscosity and σ the surface tension. For $Ca << 1$ the surface tension dominates the flow and for $Ca \gtrsim 1$ viscous forces dominates. Most previous work has been reported at low capillary number.

Two broad categories of solution methods have been used for the mathematical description of coating flows, The first method approximates the flow using lubrication theory while the second solves the full equation of motion. Lubrication theory has been shown to give reasonable agreement with experimental data for the region closest to the approach between the

rolls [4], however, for the downstream region where the liquid film splits into two, the flow is two-dimensional and the rectilinear streamlines assumed by the lubrication approximation do not hold. An extension to lubrication theory used to overcome this shortcoming is to adopt some boundary conditions at the film split point, the simplest choice being to set the pressure and the pressure gradient at the film split to zero (*Reynolds' boundary condition*). An improvement to this condition is to set the pressure at the film split location to a sub-ambient value, due to capillary pressure jump associated with the meniscus curvature as proposed by Schneider [11]. However, an extra condition is then required to determine the location of the meniscus. Savage [14] used a condition postulated by Hopkins [15] to locate the film split at the first stagnation line downstream of the plane through the centres of the rolls and midway between the roll surfaces. Coyle *et al.* [4] extended this idea to the asymmetric case, postulating that the film split line is located at the point where both the velocity and its derivative in the direction perpendicular to the flow vanish. Gaskell *et al.* [16] modified this condition and located the film split at the point at which both velocity components vanish. Another approach is to use an approximate solution of the Navier–Stokes equations at the meniscus [17] and set the boundary condition at the film split [14, 18]. Kubota and Scriven [19] introduced a visco-capillary model to describe film splitting. In the visco-capillary model, the flow near the meniscus is approximated by the Landau–Levich equation, as modified by Deryagin and Levi [20], to mimic the flow of liquid out of a pool by a roll that dips into it, and elsewhere the flow was approximated by lubrication equations. The meniscus profile from this model, however, is not accurate, because it does not account for the evolution of the meniscus shape. As well, the Landau–Levich equation is only valid for capillary number less than about 0.01, and thus the visco-capillary model, which relies on this equation, is quite limited.

Coating flow hydrodynamics is a free surface problem that is both interesting and challenging to solve. Although the flow equations are relatively easy to solve, the shape of the solution domain is *a priori* unknown. Therefore, the solution must be determined in some iterative manner, in which the domain shape evolves from an initial guess towards the final position. In the literature, several methods have been used. These methods include spines [21] elliptic meshes [7], moving meshes [22] and successive approximation [23]. In the method of spines, the free surface is represented parametrically by using a number of spines conveniently placed on the surface and included as additional unknowns in the problem. However, spines can be complicated to implement, requiring a large degree of expertise [22] and a separate scheme for placing the spines must be devised for each problem. Furthermore, if the final free surface shape is far from the initial shape from which the spines have been defined, the spines will have to be reoriented to describe the surface. Elliptic mesh generation attempts to overcome this problem by tessellating the whole domain with what may be called two-dimensional spines. However, this method requires a structured mesh, and therefore increases the number of elements excessively if the critical flow details have to be captured. Furthermore, as pointed out in Reference [7], mapping the domain into quadrangular reference regions is often difficult, and requires much mathematical complexity and experience. In the third method, the free surface is treated as part of the solution domain by employing moving/deforming mesh algorithms. The main drawback of all of these methods is that they fail unless the initial domain is close to the final solution. This requirement necessitates the use of either experimental profiles or previously converged solutions as a starting point for simulation. Furthermore, because the location of the free surface is an additional unknown, the size of the problem is increased. The successive approximation scheme is conceptually straightforward to implement. In this

method an initial domain is assumed, and the free surface is adjusted to achieve a correct force balance using some pseudo-time stepping scheme. Although the first reported finite element solution of free surface problems was based on such a scheme by Nickell *et al.* [23], these methods were widely discarded owing to the excessive execution times required as well as high re-meshing costs.

A common theme in all of the methods used is the requirement of a good initial guess combined with an efficient and robust solution methodology. In turn, an efficient domain discretization method is also a necessity. In this work, we propose a finite element solution of the Navier–Stokes equations based on the Uzawa algorithm [24]. We show a method for rapidly determining a good initial solution domain based on the Landau–Levich and Prandtl–Hopkins conditions. Following determination of the best initial guess for the meniscus location, we use the successive approximation method combined with adaptive re-meshing using a non-uniform mesh. It will be shown that this methodology yields a fast, efficient and robust methodology for free surface treatment that can easily accommodate a wide range of roll speeds, gap sizes and capillary numbers. Further, it is demonstrated that the use of adaptive re-meshing does not incur a significant cost penalty, and overall the method is more straight forward than other methods.

2. SOLUTION METHODOLOGY

Solution of the hydrodynamics in the nip of a roll coater by successive approximation can be divided into four steps. These steps are: (1) assume an initial domain based on the geometry in question, (2) discretize the solution domain using an efficient meshing strategy (which will depend on the numerical method selected), (3) solve the equations in the current domain and (4) update the domain based on the computed flow field. Steps (2)–(4) are repeated until a convergence criterion is satisfied. In the following, each of these steps is discussed in turn.

2.1. Building the initial domain

We emphasize that a key advantage of our method is that a good initial estimate for the domain is not required. Indeed, one can arbitrarily select both the initial split point position and the thickness of the fluid on the rolls. However, we can utilize the classical Landau–Levich equations, as modified in Reference [20], to provide some guidelines. The Landau–Levich equation (see Figure 2 for details) relates the radius of curvature of the meniscus and the height of the film on each roll

$$H_1 = 1.34Ca^{2/3}\left(\frac{2S}{S+1}\right)^{2/3} R_s \quad \text{and} \quad H_2 = 1.34Ca^{2/3}\left(\frac{2}{S+1}\right)^{2/3} R_s \tag{2}$$

where S is the speed ratio (U_2/U_1), H_1 and H_2 are the bottom and top layer thickness, respectively, and Ca is the capillary number based on the average speed between the rolls. It follows from Equation (2) that the film thickness ratio depends on the velocity ratio as follows:

$$\frac{H_1}{H_2} = \left(\frac{U_1}{U_2}\right)^{2/3} \tag{3}$$

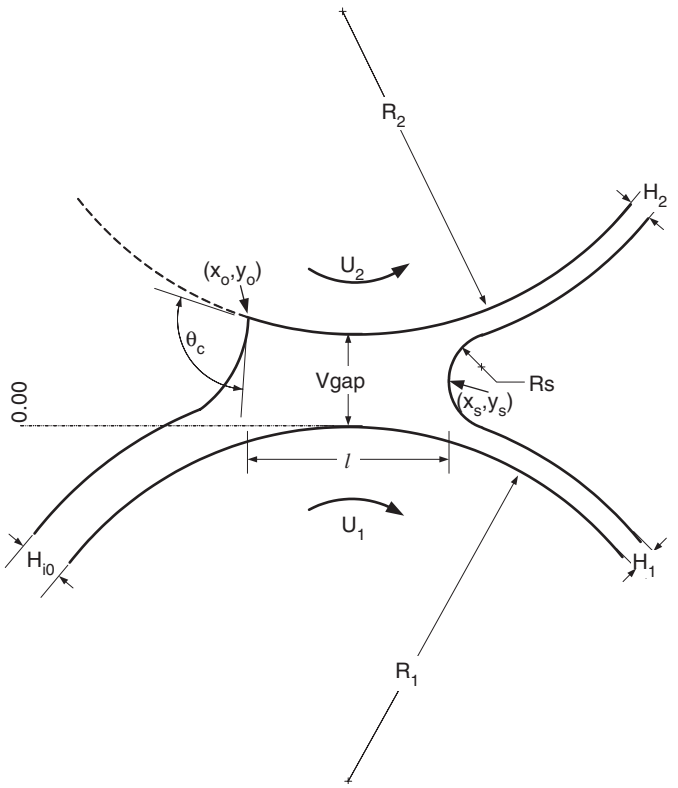

Figure 2. Roll nip configuration and nomenclature. L is the length of the nip; V_1 and V_2 are the bottom and top roll speeds, respectively; x_s, y_s is the split point location; R_S is the meniscus radius; V_{gap} is the vertical gap; θ_c is the contact angle, x_0, y_0 is the contact coordinate, R_1 and R_2 are the bottom and top roll radii, respectively; H_{i0} is the height of the incoming fluid and H_1 and H_2 are the final thickness of the exit coating on the bottom and top roll, respectively.

Equation (3) agrees with the solution of the full Navier–Stokes system, as shown by Coyle *et al.* [4]. The total height, $H_1 + H_2$, is set equal to the minimum gap (flooded nip) or the incoming fluid height (starved nip). We then assume an arbitrary film split position, X_S, and impose the meniscus as an arc of a circle that is tangent to the uniform films where it joins them. The total roll separation, $H(X_S)$, is known at the selected film split point, and thus the meniscus radius is calculated from

$$H(X_S) = 2R_S + H_1 + H_2 \tag{4}$$

We note that an initial guess for the meniscus radius can be calculated from Equation (2), however, because the Landau–Levitch equation is only valid at low capillary numbers this estimation was not done. As we shall demonstrate, our initial domain positioning method is sufficiently rapid to render an estimate of R_S unimportant.

2.2. Mesh generation

The difference in the size and shape of the domain between the initial guess and the final converged solution can be very large. Use of a single mesh for all successive solutions with internal node displacement can thus lead to a distorted mesh, with a subsequent loss of accuracy. This would be especially true when a fine mesh is imposed around the free surface boundaries, which is desirable to capture well the flow features. We therefore adopted a strategy of adaptive domain re-meshing after each iteration. A non-uniform mesh was used, where the local element size was adjusted heuristically according to the shape of the domain. In this way, we could preserve well shaped elements, with small elements along the boundary, larger elements in the interior, and at the same time minimizing the total number of elements. The element size was chosen to be as large as possible without affecting the solution.

There are many commercial mesh generators available, and the governing factor for selection is the control over local mesh refinement and ease of integration into the overall solution scheme. We chose ARANEA, a robust unstructured generator developed by Marchand *et al.* [25]. ARANEA is very robust and offers excellent control over mesh refinement. Mesh refinement is very critical in this process to capture the flow outline at the critical zones, i.e. the film split region as well as the three phase contact point. The flow structure at the critical points can only be captured adequately by concentrating the mesh density at those points where there are steep gradients in velocity and pressure. At the same time, it is desirable to use as large an element as possible to minimize overall execution time. Figure 3 shows a typical mesh size distribution at the critical points of the coating flow regime, which are (a) the exit zone and (b) the contact point. ARANEA can perform automatic mesh generation and refinement without having to visualize the mesh generation process at each iteration. The mesh size was adapted heuristically, incorporating on the degree of movement of the domain.

Note: When re-meshing between iterations, it is possible to interpolate the solution from the 'old' to the 'new' mesh. By having a better initial guess, the number of fixed-point iterations required (see Section 2.7) is reduced. However, in this work, it was found that the penalty paid to compute the interpolated solution exceeded the speedup achieved by a reduction in the number of fixed point iterations, and was thus not used.

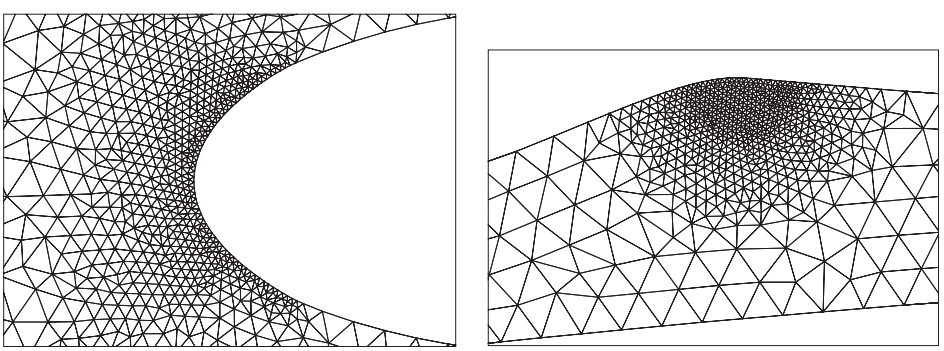

Figure 3. Plot showing typical mesh refinement at critical points: (a) outlet; and (b) inlet.

2.3. Flow equations

Steady laminar fluid flow is governed by the equation of motion

$$\rho \mathbf{u} \cdot \nabla \mathbf{u} - \nabla \cdot \boldsymbol{\tau} = \rho \mathbf{g} \tag{5}$$

and the continuity equation of mass conservation

$$\nabla \cdot \mathbf{u} = 0 \tag{6}$$

where ρ is the fluid density, $\mathbf{u}$ its velocity and $\boldsymbol{\tau}$ the total stress tensor. For a Newtonian fluid, the total stress tensor is related to the local hydrodynamic pressure, p, and the strain rate by

$$\boldsymbol{\tau} = -p\delta + 2\mu\dot{\gamma} \tag{7}$$

where

$$\dot{\gamma} = \tfrac{1}{2}[\nabla \mathbf{u} + (\nabla \mathbf{u})^{\mathrm{T}}] \tag{8}$$

For a non-Newtonian fluid, Equation (7) is replaced by an appropriate equation incorporating a rheological model to depict the non-linear viscosity of the liquid. The boundary conditions for Equations (5)–(7) are presented in the next section.

2.4. Boundary conditions: fluid solid interface

Figure 4 shows the boundary conditions used in forward roll coating flows. As shown, the boundary conditions can specify velocity, traction or a functional relationship between them.

For all boundaries where the fluid is in contact with a solid surface, the liquid velocity is assumed to be the same as that of the solid surface, i.e. no slip conditions

$$u = U_{\text{solid}} \tag{9}$$

At the point where gas, solid and liquid appear to intersect (three phase contact point in Figure 5(a), the no-slip hypothesis and 2-D steady flow leads to infinitely high stresses [26–28]. Replacing the no-slip condition in the vicinity of the contact line with some form of slip condition has been shown to be a sufficient stopgap measure to alleviate the singularity. Navier's slip condition, which makes the velocity discontinuity proportional to the shear stress at the solid surface, is widely used

$$\frac{1}{\beta}\mathbf{t} \cdot (\mathbf{u} - U_2) = \mathbf{tn} : \boldsymbol{\tau} \tag{10}$$

where β is the slip coefficient ($\beta \to 0$ corresponds to no slip conditions and $\beta \to \infty$ corresponds to a shear free boundary condition), $\mathbf{t}$ and $\mathbf{n}$ are the unit vectors tangent and normal to the surface, respectively, and U_2 is the velocity of the top roll. The flow in the vicinity of the contact line is not completely understood. Recent investigations focused on determining the dynamics near the contact lines [27]. Dussan [28] showed that the particular form of distribution of slip is of secondary importance, but the slip length introduced has an effect on the overall flow field. We therefore adopted a simple linear distribution for the current study

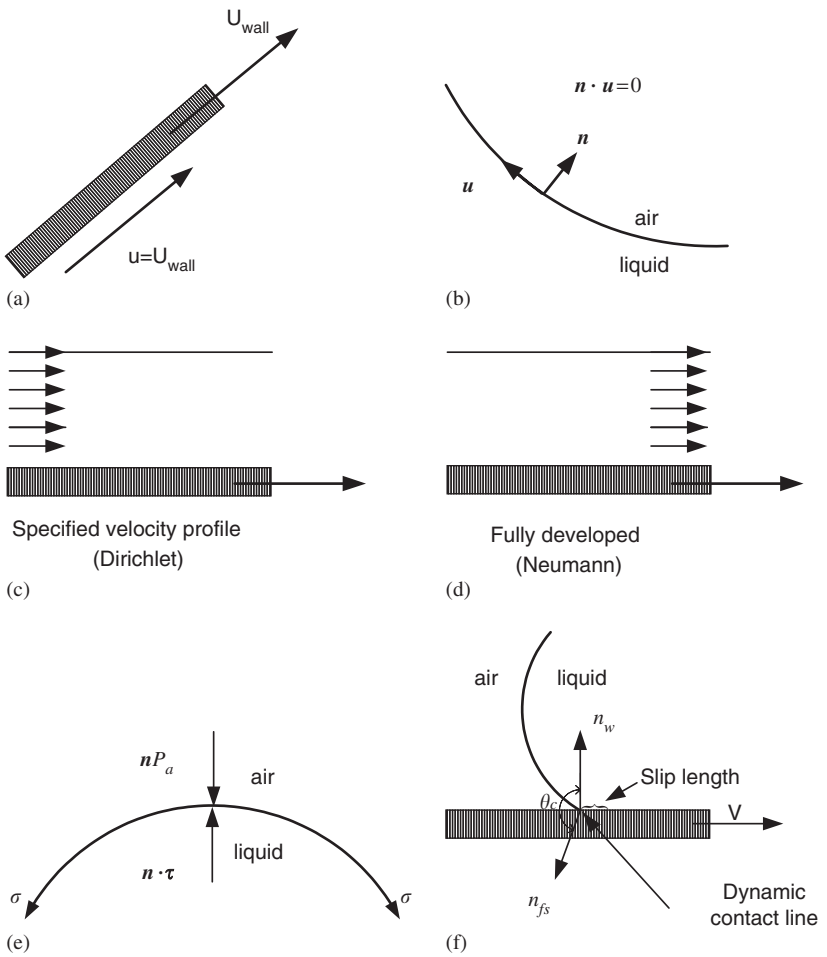

Figure 4. Boundary conditions for coating flow simulation: (a) no-slip; (b) kinematic; (c) inflow; (d) outflow; (e) capillary pressure; and (f) dynamic contact line.

where the slip velocity is

$$\mathbf{u} = \begin{cases} U_2 \left(\dfrac{x - x_0}{l_S} \right) & \text{for } x_0 \leqslant x \leqslant x_0 + l_S \\ U_2, & x > x_0 + l_S \end{cases} \tag{11}$$

Here, l_S is the slip length (chosen as five microns), x_0 is the coordinate of the attachment point and U_2 is the roll speed.

Either the position of an apparent dynamic contact line has to be specified or the inclination of the free surface at the place specified by a contact angle, θ_c, see Figure 4(f). Some authors specify both parameters [22, 29, 30]. The contact angle is usually found by experiment and a

value of $\theta_c = 95$–160° has frequently been used for a rigid roll/Newtonian fluid [29]. In the method proposed here, the contact point is pinned at the surface during flow resolution and then its position updated iteratively by an amount that depends on the movement of the free surface; that is, the contact angle adjusts naturally.

2.5. *Boundary conditions: inflow regimes*

The nip region merges into simpler inflow and outflow regimes upstream and downstream, respectively, as shown in Figure 5(a). The inflow boundary condition has to be considered in the context of the physical situations that can exist, which in turn depend on the feed rate to the nip and the maximum flowrate possible in the nip. The maximum flow through the nip

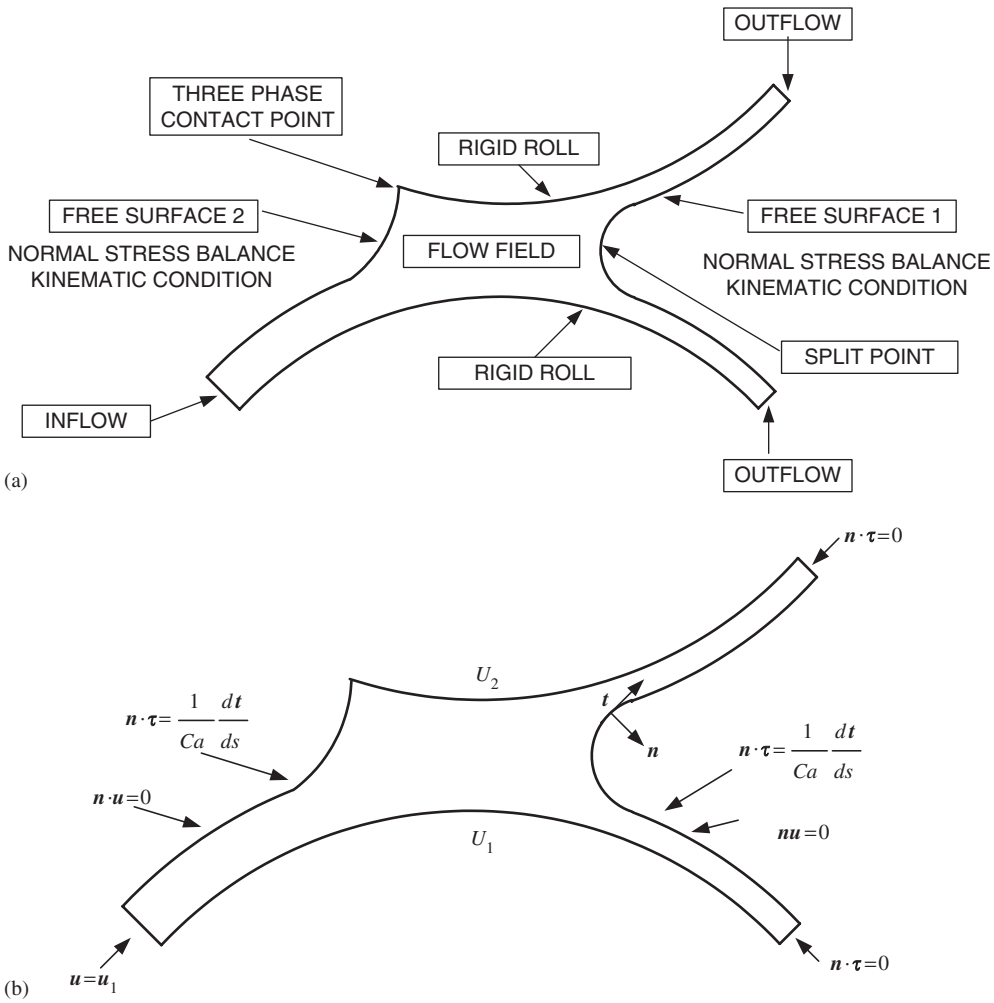

Figure 5. 2-D boundary conditions applied in forward roll coating with free boundaries: (a) designations; and (b) equations.

is determined by the roll speed and the nip gap. If the incoming fluid height is pre-metred with a flowrate less than the maximum, the nip is in the starved regime. For this case, the incoming fluid height is fixed and a Dirichlet condition is imposed at the inlet. For pre-metred flows where the fed flowrate is greater than the maximum, or the fluid is drawn by the rolls from a reservoir, the nip operates in the flooded regime. For a pre-metred flow greater than the maximum, some runback or accumulation will occur at the inlet. In this case, the free boundary condition proposed by Papanastasiou *et al.* [31] for synthetic outflow conditions can be used. Essentially, the nodes at the inlet plane are left as unknowns (no boundary conditions applied). There are two options in applying this condition. One may simply flood the nip and impose the condition across the entire inlet region, or impose it across the inlet fluid height on the roll [7]. The latter choice implies a runback along the entire incoming fluid layer, the thickness of which is *a priori* unknown. Alternatively, one may impose a fixed incoming fluid height and a Dirichlet condition, however, in this case conservation of mass requires that the formation of a stable incoming free surface is not possible. In practice, in applications with a pre-metred flow that gives a flooded nip, the excess fluid is removed using a doctor blade. To simulate this scenario, we will show that it is sufficient to use the free boundary condition for fully flooded as well as starved nip.

2.6. Boundary conditions: outflow regimes

If we assume that the flow is fully developed at the outlet, see Figure 4(d), we can impose a free boundary (Neumann) condition.

2.7. Boundary conditions: free surfaces

At the free surfaces, two conditions must be satisfied, namely the balance between fluid traction and capillary pressure, and the conservation of mass. By using successive approximation techniques, these conditions can be satisfied iteratively, i.e. one of the conditions is applied for the flow field resolution and the other condition is used in the successive approximation of the free surface. A convergence criterion is set such that the final solution is obtained when both conditions are fully satisfied at the free surfaces.

If the gas is assumed to be both inviscid and inertialess, the shear stress will vanish at the gas/liquid interface. Therefore, the total normal stress in the liquid (pressure plus viscous forces) must balance the sum of gas pressure and the normal resultant of surface tension acting in a curved surface (capillary pressure, Figure 4(e)), which is expressed mathematically as

$$\mathbf{n} \cdot \boldsymbol{\tau} = \frac{1}{Ca} \frac{\mathrm{d}\mathbf{t}}{\mathrm{d}s} - \mathbf{n} P_{\mathrm{a}} \tag{12}$$

The capillary number, Ca, is the ratio of viscous to surface tension forces, defined in Equation (1), and s is the distance measured along the free surface. If there is no flow through the liquid/gas interface, the free surface is a streamline, that is

$$\mathbf{n} \cdot \mathbf{u} = 0 \tag{13}$$

2.8. Flow field resolution

Equations (5) and (6) were solved using the Galerkin finite element method. We employed the triangular Crouzeix–Raviart element, which uses enriched quadratic polynomial basis functions

for the velocity, and discontinuous linear function for the pressure. This element has been shown to satisfy all conditions for compatibility and stability [32]. The treatment of the nonlinearity was handled by a quasi-Newton method whereby the global Jacobian matrix was built and factorized only once, and used in the fixed-point iterations of the Uzawa algorithm [24] that enables the computation of the velocity and pressure in a decoupled fashion:

0. Given $p^{(0)}$ and $\mathbf{u}^{(0)}$
1. For $n = 0, 1, 2, \ldots$ until convergence

1.1. Solve for $\mathbf{u}^{(n+1)}$

$$-\mu\nabla^2\mathbf{u}^{(n+1)} + \rho u^{(n+1)} \cdot \nabla\mathbf{u}^{(n)} + \rho u^{(n)} \cdot \nabla\mathbf{u}^{(n+1)} + r \cdot \nabla(\nabla \cdot \mathbf{u}^{n+1}) = \rho\mathbf{g} - \nabla p^n \tag{14}$$

1.2. Compute $p^{(n+1)}$

$$p^{(n+1)} = p^{(n)} + r \cdot \nabla\mathbf{u}^{(n+1)} \tag{15}$$

In this algorithm, r is a constant that should be large enough. In this work, when setting $r = 10^6$, $\mathbf{u}^{(0)} = (0, 0)$ and $p^{(0)} = 0$, this generalized Uzawa algorithm, which combines the standard Uzawa algorithm and a quasi-Newton method, required about three fixed-point iterations to converge.

When the above calculations have converged to a tolerance of 10^{-4}, the positions of the free surface nodes can be updated using the selected free surface updating procedure, which is discussed in a subsequent section.

3. DOMAIN DETERMINATION

The solution of the equations and boundary conditions given in Section 2 describes the hydrodynamics in the coating nip. However, the solution domain is *a priori* unknown. We therefore need to adopt some form of iterative method to determine the final shape from an arbitrary initial guess.

The solution methodology used here may be called 'successive approximation' or 'iterative procedure' for free surface flows. In successive approximation, one assumes an initial domain geometry, usually based on the roll radii and an estimate of the film split point (exit free surface) and three phase dynamic contact line (inlet free surface). The flow equations are then solved and the domain modified according to the boundary conditions on the free surface. At the free surfaces, one of the two boundary conditions is used to obtain the flow solution. The other boundary condition is utilized afterwards to update the location of the free surface. The new position of the free surfaces may then be smoothed and used to create a new outline. This procedure is repeated successively until all conditions are satisfied, i.e. the newly created surface is no different from the previous surface.

3.1. Optimizing the initial meniscus position

The main disadvantage of the traditional successive approximation method is the requirement for gradual surface displacements to preserve the stability. This requires that the pseudo-time step (used in Equation (17), see Section 3.2) be small enough to avoid excessive distortion of the free surface. As a result of the use of a small pseudo-time step, the scheme is very

slow to converge [21, 33], especially when the initial estimate of the film split point is far from the final position. It is therefore imperative to obtain a good estimate of the position of the free surface before we start the successive approximation method. To achieve this, we introduce a new approach that we call prescribed initial domain stepping (PIDS).

The prescribed initial domain stepping method involves successive estimations of the flow-split location to find an approximate location close to the final solution. Starting with an arbitrary location and shape of the outlet free surface (in this work we start with a semi-circle), the flow field parameters are computed. The location of the initial free surface is then adjusted by moving the split point in the direction of its velocity component along the nip axis by an arbitrary amount. The shape of the free surface is maintained as a semi-circle. This procedure was repeated until the sign of the velocity component at the split point changes, signifying that the final flow split location has been exceeded. The location of the equilibrium (final) split point is then known to lie within a narrow range, and successive iterations are then allowed to proceed. After this point, the free surface shape and location are allowed to adjust themselves successively. Mathematically, this process is equivalent to seeking a point in the vicinity of the flow separation point as described by the Prandtl–Hopkin condition, i.e.

$$u_x = \partial u_x = 0 \tag{16}$$

3.2. Updating the free surface

When the flow equations have converged to a tolerance of 10^{-4} for a fixed domain, the positions of the free surface nodes were updated using the selected free surface updating procedure. Two procedures were implemented, depending on the type of boundary condition used to obtain the field values, i.e. a kinematic movement scheme was used when normal stress conditions have been applied earlier as boundary conditions, and the normal stress scheme was used if the kinematic conditions were applied at the free surfaces as boundary conditions. The two schemes are outlined in the next sections.

3.3. Kinematic movement scheme

If the normal velocity components computed for nodes at the free surfaces are U_{nx} and U_{ny}, respectively, the free surface nodes will be moved according to the following formulae:

$$\begin{aligned} x^{i+1} &= x^i + \alpha U_{nx} \\ y^{i+1} &= y^i + \alpha U_{ny} \end{aligned} \tag{17}$$

where α is a pseudo-time step whose size was determined heuristically to give a stable solution. In this work the value was typically 10^{-6}. The new positions of the free nodes may then be spline smoothed and used as the basis for a new computational domain. The only node that may not belong to the free surface, but has to be moved, is the three phase contact point on the inlet free surface. The contact point was not moved as part of the free surface movement algorithm, but rather was located by projecting the free surface onto the roll as shown in Figure 6.

Another scheme implemented within this methodology is to move all points on the free surface by solving a 1-D finite element problem along the free surface. This scheme is based on an adaptive nodal displacement procedure. Here, the displacement is an unknown, which

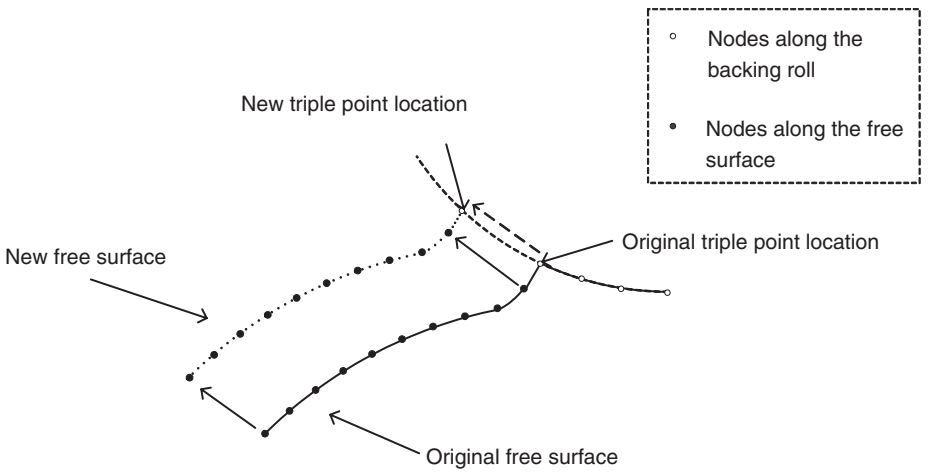

Figure 6. Projection of the triple point along the top roll surface.

is solved for using a weak variational form of the boundary conditions [34, 35]. The method is outlined in the following paragraphs.

Define ξ as a unit displacement vector that can be oriented normal to the surface or in the direction of velocity along the free surface. If each free surface node (denoted with subscript 0) is moved to new position, then we may write

$$\begin{aligned} x &= x_0 + h\xi_x \\ y &= y_0 + h\xi_y \end{aligned} \tag{18}$$

where h is the displacement length. We define J as a variational factor along an arc length

$$J = \left(\left(\frac{\mathrm{d}x}{\mathrm{d}s} \right)^2 + \left(\frac{\mathrm{d}y}{\mathrm{d}s} \right)^2 \right)^{1/2} \tag{19}$$

It can be shown that the normal to the free surface curve is given by

$$\mathbf{n} = \mathbf{n}_0 + hJ^{-1} \frac{\partial \xi^{\perp}}{\partial s} - J^{-1} \frac{\partial h}{\partial s} \xi^{\perp} \tag{20}$$

where $\xi^{\perp}$ is the vector orthogonal to ξ, and $\mathbf{n}_0$ is the current normal to the free surface. We can therefore write the kinematic boundary conditions as

$$\mathbf{u} \cdot \mathbf{n}_0 - h\mathbf{u} \cdot J^{-1} \frac{\partial \xi^{\perp}}{\partial s} - J^{-1} \frac{\partial h}{\partial s} \mathbf{u} \cdot \xi^{\perp} = 0 \tag{21}$$

Equation (21) is then written in the weak form and solved for h using the Garlekin finite element method. In this case, the free surface movement between each successive iteration is much gentler. However, the time taken for this solution is greater than that with movement of each node separately using the pseudo-time step approach.

3.4. Normal stress movement scheme

In the normal stress movement scheme, the resultant normal stress after computation is balanced with the capillary stress to give a net force, which is used in turn to move the surfaces in such a way that the final position of the free surface will correspond to a balance between the fluid stresses and the capillary stresses acting at the free surfaces.

For the equilibrium between hydrodynamic and capillary stresses along the free surface, the following relation has to be satisfied:

$$(\boldsymbol{\tau}_{\mathrm{F}} - \boldsymbol{\tau}_{\mathrm{C}}) \cdot \mathbf{n} = 0 \tag{22}$$

where $\boldsymbol{\tau}_{\mathrm{F}}$ is the hydrodynamic stress and $\boldsymbol{\tau}_{\mathrm{C}}$ the capillary stress along the free surface. Thus if we calculate the hydrodynamic stress tensor from Equation (7) as

$$\boldsymbol{\tau}_{\mathrm{F}}^{(n+1)} = -\, p^{(n+1)}\delta + 2\mu\dot{\gamma}(\mathbf{u}^{(n+1)}) \tag{23}$$

the normal projection of the hydrodynamic stress tensor, $F^{(n+1)}$, is

$$F^{(n+1)} = \boldsymbol{\tau}_{\mathrm{F}}^{(n+1)} \cdot \mathbf{n} \tag{24}$$

The capillary stress vector is

$$C^{(n)} = \boldsymbol{\tau}_{\mathrm{C}} \cdot \mathbf{n} = \frac{1}{Ca}\frac{\mathrm{d}t}{\mathrm{d}s} - \mathbf{n}P_{\mathrm{a}} \tag{25}$$

The residual stress on the free surface is given by

$$F_{\mathrm{res}}^{(n+1)} = F^{(n+1)} - C^{(n)} \tag{26}$$

Assuming a linear displacement, we can calculate the corresponding movement of the node due to the force imbalance, and therefore update the different positions as

$$x^{(n+1)} = x^{(n)} + \omega F_{\mathrm{res}}^{(n+1)} \tag{27}$$

where ω is a stiffness constant and $F_{\mathrm{res}}^{(n+1)}$ the residual force. The stiffness constant was chosen heuristically to obtain a stable movement. Here, we used a value of 10^6. We now describe some of the critical issues that must be addressed to develop a robust simulator.

3.5. Movement schemes and the convergence criteria

The choice of movement scheme is governed by, among other things, the range of capillary numbers for the problem at hand. For cases where the capillary number is high, it is found best to apply the normal stress conditions for the solution of the flow field and to use kinematic conditions to adjust the free surfaces. For cases where the capillary number is very low (less than 0.1), it is best to apply the kinematic conditions for flow field resolution and to use normal stress condition to move the free surface. For intermediate values ($0.1 < Ca < 1$) either of the schemes can be used. Both of these options were implemented in the software.

To test the convergence of the free surface, we used a dimensionless parameter, Ψ, that relates to the characteristic velocity of the free surface and the average roll speed, U as

$$\Psi = \frac{\sum_{j=1}^{N} u_n^j}{NU} \tag{28}$$

where N is the total number of nodes in the free surface and u_n^j is the normal velocity at node j. The free surface is converged when the parameter Ψ is smaller than a prescribed tolerance.

4. NUMERICAL RESULTS

4.1. Outlet free surface development

In this section we show some numerical results for the inlet and outlet free surfaces. We start by illustrating the initial domain stepping scheme. Two simulations are illustrated, both with the initial guess far from the final solution. In one case, the initial flow-split point was close to the nip and in the other case it was far from the nip. The movement of the initial meniscus in each case is shown in Figure 7, where it is seen that approaching from either extreme gives approximately the same endpoint. Once an initial good estimate was obtained, the free surface evolves according to the standard successive iteration method, described in Section 3.

Following successive approximations, the shape of the free surface at the flow-split (stagnation point) will no longer be the semi-circle assumed during the initial domain stepping phase; rather, the shape adjusts itself to satisfy the boundary conditions, as shown in Figure 8. It should also be noted that the split point moves, though not a great distance, indicating that a good initial estimate was provided in the initial domain stepping phase.

Figure 9 shows the corresponding vector field (a) when the meniscus shape is still semicirclular, and (b) the final shape of the meniscus which is more elliptic. As expected, the free surface is a streamline when all conditions are fully satisfied. Although the number of steps taken to reach the converged solution will vary with initial solution and the operating conditions, for this case the solution took about 28 000 iterations to reach the solution using the standard iteration method, but only 30 with our initial domain stepping applied. It

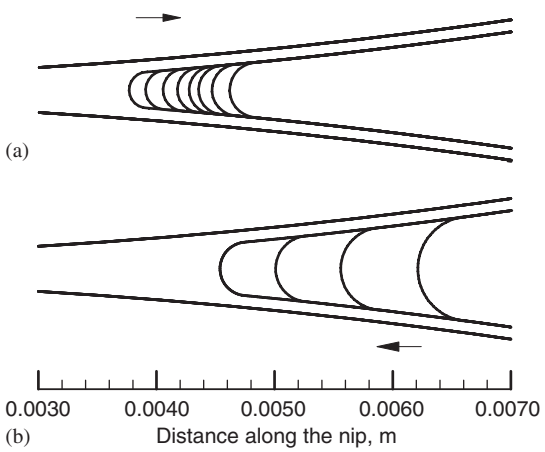

Figure 7. Domain stepping approach from two extreme initial guesses.

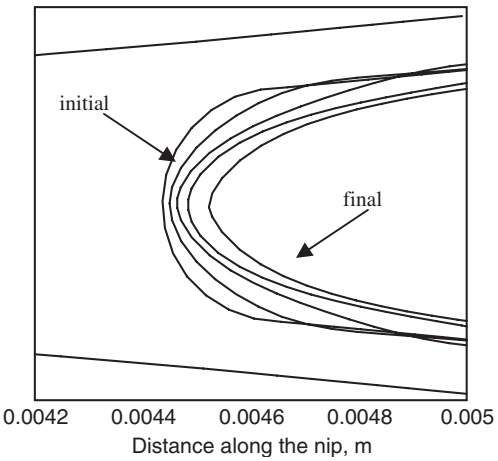

Figure 8. The progression of development of the final meniscus shape starting from a circular meniscus.

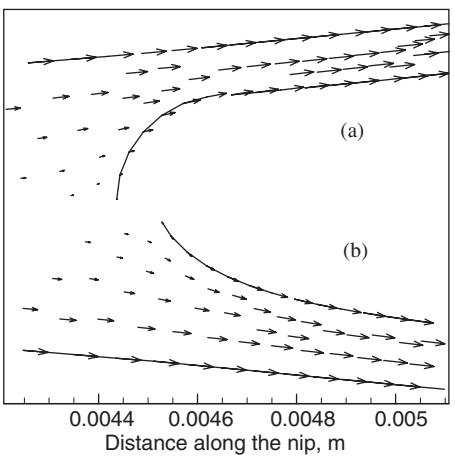

Figure 9. Vector fields showing velocity vectors: (a) before; and (b) after final convergence. One half the nip height is shown in each case.

is evident that the initial domain stepping procedure reduces the number of free surface iterations required by up to three orders of magnitude, and thus the successive iteration method is computationally viable.

Figure 10 shows the corresponding velocity streamlines for a converged solution. It is clear that the free surface is a streamline and the flow-split point is stationary.

Typically, the initial stepping phase took 3–5 steps to obtain a free surface that was less than 5% from the final split point location. About 20–40 free surface iterations were then required to allow the free surface to evolve so as to reach a prescribed tolerance of less than

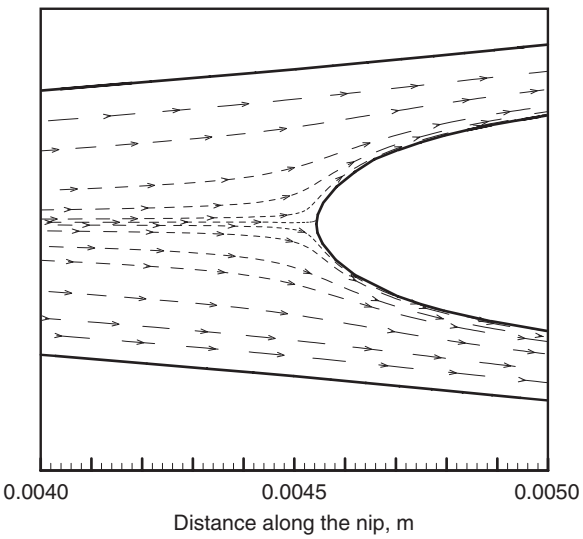

Figure 10. Velocity streamlines for a fully converged solution.

0.3%. For each problem, the initial number of elements was 1200 during the initial stepping phase. This number was then doubled to about 2000 elements and allowed to increase with readjustment, with the final mesh having 2900–3000 elements when the final solution was obtained. Further increase in the number of elements did not improve the solution. A single free surface approximation with a fine mesh step took about 10 s on a 2.4 GHz XEON. This means that the average total time for complete solution of any of the problems investigated in this work was less than 10 min, regardless of the initial starting point.

4.2. Flow dynamics of the upstream bank

The upstream bank may be fully flooded or starved to different degrees. Many investigations on forward roll coating have concentrated on the front (meniscus) dynamics with the assumption that the back end is essentially flooded, or that the backend does not affect the fluid mechanics of the exit point. It is obvious that there is a range of operating conditions where this is not the case. When the height of the incoming fluid is less than the minimum gap separation, we have starved coating, which has been studied both experimentally and numerically by, for example, Gaskel *et al.* [36]. We illustrate here the behaviour of the inlet under flooded and starved conditions.

Consider the case in which the incoming fluid height is given some value. Essentially, as noted above, two situations are possible. When the height of the incoming fluid is equal to or less than the gap width, the attachment point will stabilize at a final position. This behaviour is shown in Figure 11. Figure 11(a) shows the evolution of the inlet free surface from the initial guess to the final position, while Figure 11(b) shows the streamlines of the flow. For the equal roll speed and roll sizes, which were investigated here, the maximum film thickness is a function of the gap clearance. When the incoming film (H_{i0}) is less than the minimum

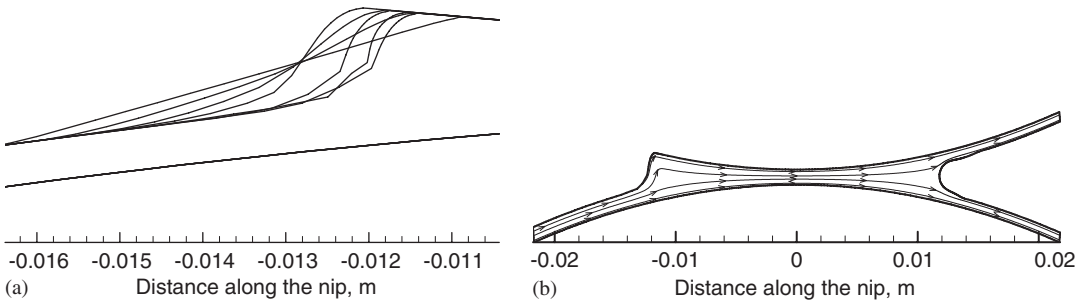

Figure 11. Simulation with incoming fluid height equal to the nip gap: (a) development of the free surface shape; and (b) velocity streamlines.

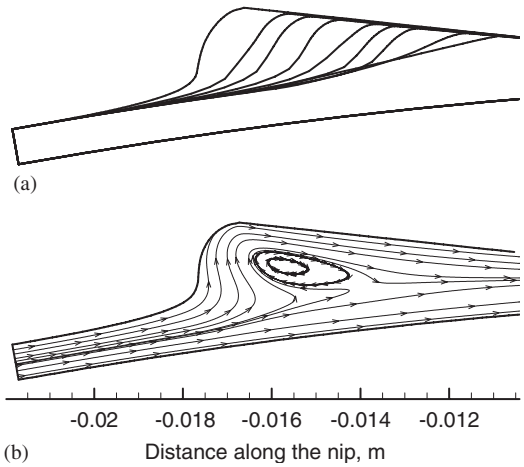

Figure 12. Development of the attachment point with pre-metred height greater than the nip gap: (a) inlet meniscus progression; and (b) streamlines showing an unstable gyre.

gap, the outlet film thickness depends on the incoming height thickness. It should be noted that for a given gap, there is a minimum incoming thickness for which a stable coating bead may be formed. However, this limit was not investigated in this study. On the other hand, if the incoming layer is just about or slightly higher than the minimum gap, the outlet meniscus depends on both upstream and downstream conditions. In this case, the attachment point as well as the flow split point oscillate over a small range of positions (not shown). In this case, a single solution is not possible, unless one of the positions is fixed.

When the incoming height is greater than the gap width, part of the incoming fluid will return (runback) and a gyre forms at the entrance. Figure 12 illustrates the latter case. Figure 12(a) shows the evolution of the attachment point as free surface approximation proceeds in our simulations; the free surface continues to move to the left, and does not stabilize.

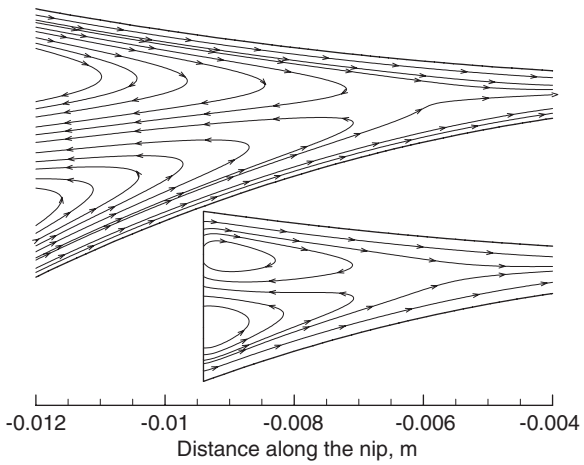

Figure 13. Synthetic inlet conditions using the free boundary condition for two differently sized inlet domain sizes. Beyond a short distance from the inlet the streamlines correspond.

Figure 12(b) shows the formation of the gyre in the inlet region. In this situation, part of the incoming fluid will pile up at the front of the nip gap. In practice, this is the amount that has to be scraped off using a doctor blade. For the case of simulation, we see a pile of fluid accumulating at the front end without obtaining a single converged solution.

To allow for the range of inlet states covering both starved and runback flows, the boundary condition at the inlet was changed from specified velocity to the free boundary condition discussed in Section 2.5. This condition was used by Carvalho and Scriven [7] in their investigation of the inlet flow. With this boundary condition, it was possible to investigate the entire range of inlet conditions. The main difference with our approach compared to that of Carvalho and Scriven [7] is that there is no need to match the kinematic and the free inlet conditions, because this is done automatically at each step by specifying kinematic conditions on the free surface during the free surface movement process. In other words, a Neumann inlet boundary condition gives the same result as the specified velocity (Dirichlet condition) provided that no runback through the inlet occurs. Thus, for a pre-metred flow with a sufficiently long inlet length, such that no runback occurs through the inlet, the velocity profile across the inlet is uniform. Ultimately, liquid pileup at the inlet will always result in a runback through the inlet, and thus specifying a free inlet condition will satisfy all cases.

For the case of runback flow, the nip is flooded, and thus one can disregard the upstream bank and simply use the free boundary condition. Rather than specify some inlet length, one can simply specify a flooded inlet with an arbitrary domain. The domain size is not important, as shown in Figure 13. Figure 13 shows the application of free boundary condition for an inlet-flooded domain with two different synthetic inlet domains. The flow streamlines for both domains are the same, except for minor differences at the inlet plane, and it can be concluded that this is a sufficient condition to apply in the case of flooded inlets, and that the size of the domain is not critical, provided that a certain minimum size is specified.

5. COMPARISON OF SIMULATION WITH EXPERIMENTS

We have described in the foregoing the development of a robust, efficient and automatic method for the simulation of forward roll coating flows. The simulator has been tested over a wide range of operating conditions, which encompassed the range of capillary numbers from 0.01 to 300, and nip gaps up to 1 mm. In this section, we compare simulation results to experiments taken from the literature. We are restricted to relatively small capillary numbers (up to about 1) owing to a lack of experimental data at high capillary numbers. These model validations take the form of meniscus shapes and pressure profiles. There is a paucity of experimental data for rigid roll coating in the literature with regard to meniscus shapes and pressure profiles. Some of the results will therefore be compared for the case of rigid roll/flat plate geometry instead of a roll–roll configuration.

5.1. Model validation: meniscus profiles

An extensive set of experimental meniscus profiles reported in the literature [9, 10] provides a good test for the above procedure. In that work a Newtonian fluid was used with two rigid rolls. The rolls had different sizes, and a variety of operating conditions were reported. An argon laser sheet was applied to the fluorescent fluid to enable video recording of the meniscus profiles. The reported experimental error in the meniscus profiles is $\pm 15\,\mu$m.

Figure 14 shows a comparison of meniscus profiles measured by laser fluorescence method [9] and simulation. The experimental conditions were capillary number of 0.14, speed ratio of 1, and a ratio of roll diameters of 2.46. The total gap width was 0.64 mm. It is seen that the meniscus shape and the flow split point were captured within the experimental uncertainty. Figure 15 shows a set of different experimental meniscus profiles obtained from laser fluorescence measurements by Decré *et al.* [10]. Here again we observe a close match between the experimental measurements and simulations for different operating conditions. There is no doubt that our meniscus location method is both rapid and accurate. It should be

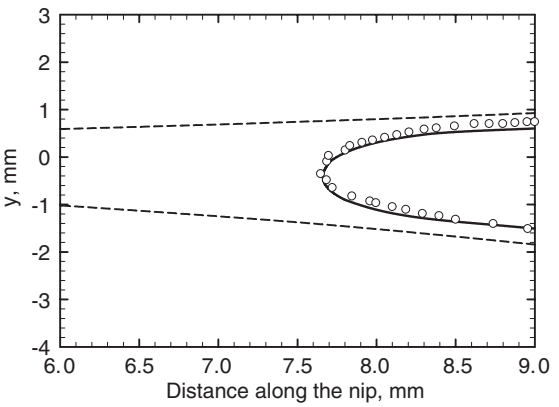

Figure 14. Comparison between numerical and experimental [9] meniscus profile ($Ca = 0.14$, $S = 1$; $R_2/R_1 = 2.46$; $2H_0 = 0.64$ mm). The points are experimental values and the solid line the simulation.

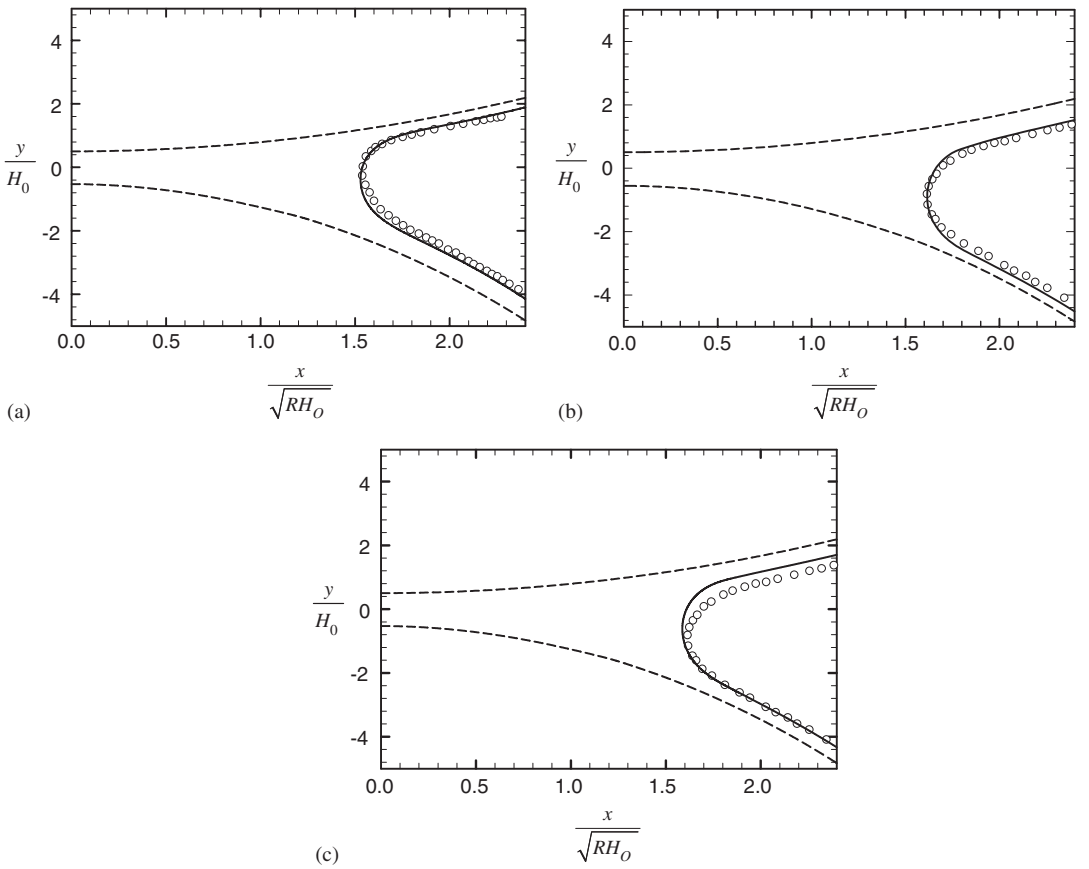

Figure 15. Comparison between experimental [10] and simulated meniscus profiles. $Ca = 0.6$, $R_1/R_2 = 2.45$, $2H_0 = 0.64$ mm. Different velocity ratio: (a) $S = 3$; (b) $S = 0.333$; and (c) $S = 1$. The points are experimental values and the solid line the simulation.

pointed out that despite the publication of the experimental data about a decade ago, this is the first time such a comparison has been made independently.

5.2. *Model validation: pressure profiles*

We illustrate two cases of pressure profiles taken from the literature. Both of these cases are for rigid rolls with flat plates. The first case is taken from Gaskell *et al.* [36]. The stationary flat plate was used to facilitate pressure measurement using capillary manometers. The experimental conditions were: roll radius of 125 mm, total nip gap 0.18 mm and capillary number of 0.3. Figure 16 shows a comparison of the pressure profiles between experiment and simulation. Generally speaking the agreement is good, and within the experimental error expected. It should be noted that this is the first time such experimental results have been simulated numerically.

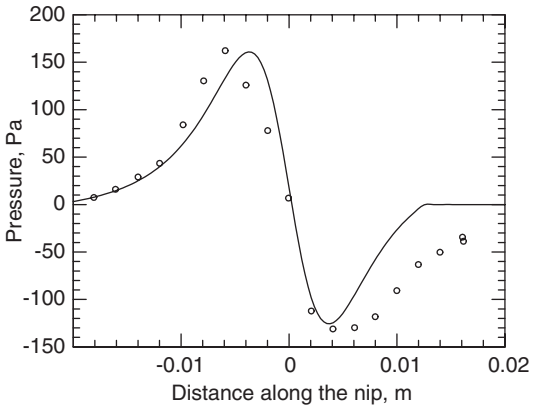

Figure 16. Comparison between simulation and experimental results of Gaskell *et al.* [36]. Flat plate and rigid roll apparatus with a roll radius of 125 mm and a total nip gap of 0.180 mm. The capillary number was 0.3.

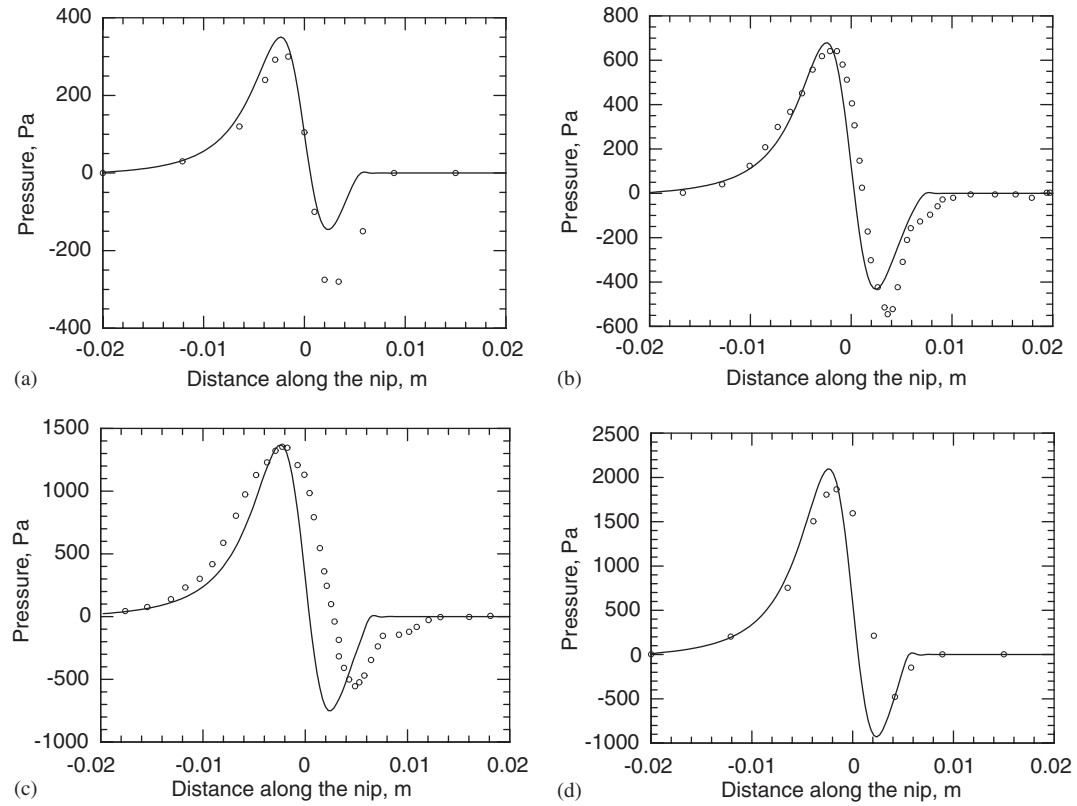

Figure 17. Comparison between simulation and experimental results of Young [37] with a flat plate and a rigid roll setup. The roll radius was 50 mm and the total nip gap 0.2 mm. The capillary numbers are: (a) 0.14; (b) 0.29; (c) 0.57; and (d) 0.86.

The second case was taken from the work of Young [37]. The experimental conditions used by Young and for the simulation were as follows. The roll radius was 50 mm, the total gap width varied from 100 to 400 μm, the roll velocity varied from 5 to 30 m/min, the fluid viscosity was 0.0562 Pa s and the surface tension 0.0326 N/m. The four cases examined corresponded to capillary numbers of 0.14, 0.29, 0.57 and 0.86. Although not stated explicitly if the flat plate was moving or not, simulation results and comparison with Gaskell's data confirms that the flat plate could not have been moving for these experiments.

Figure 17 shows a good agreement between simulation and experimental data for the roll/flat plate combination, especially for the maximum (peak) pressures. If we look at the reported maximum and minimum pressure values for all of the data shown, the minimum values do not change substantially at velocities higher than about 10 m/min for the experimental results, whilst the simulated values continue to increase as the velocity increased. This may be due to measurement artifacts, as we would expect the magnitudes to increase with increasing velocity when the bounding walls for the flow are rigid. Nevertheless, if we assume an experimental error of about 20% as stated in the thesis [37] due to pressure measurements, the results are in good agreement. There seems to be a greater discrepancy in the negative pressure loop. However, a closer examination of the experimental data reveals that the negative loop measurements are much more inaccurate. For example, the minimum peak should increase as the rotational speed is increased. However, the measured values for minimum peak seem to show insensitivity, to the speed increase, which is counter intuitive. Nevertheless, we are confident that this limited dataset demonstrates the robustness of the methodology used in this study.

6. CONCLUSIONS

A robust solution methodology for the simulation of roll coating flows with free surfaces has been developed. The method overcomes the disadvantages of other free surface approximation techniques. The need for a good initial guess for the initial solution domain has been eliminated. It is shown that the full Navier–Stokes equation is easily used in a cost effective manner. Adaptive re-meshing at each pseudo-time step in the method of successive approximations allows for the accurate capture of the free surface shape without a significant cost penalty. The correct selection of the free surface movement scheme based on the capillary number is the key to a successfully converged solution. The method has been validated against available experimental results for both meniscus shape and pressure profile taken from the literature.

NOMENCLATURE

Ca	capillary number
c_j	coefficient for the approximation of the displacement parameter
C	capillary force, N

F fluid force, N
F_{res} residual force, N
h free surface displacement parameter
H_0 half the minimum gap width, μm
H_1 height of the coating layer leaving with the bottom roll, μm
H_2 height of the top layer leaving with the top roll, μm
H_{i0} height of the initial coating layer, μm
J variational parameter in curvature formula
l length of the nip, m
l_S slip length
$\mathbf{n}$ vector normal to the free surface
p pressure, Pa
P_a ambient pressure, Pa
Q flow rate, m^3/s
Q_0 initial flow rate at the pre-metred point, m^3/s
r constant in Equation (14)
R_1 radius of the bottom roll, m
R_2 radius of the top roll, m
R_S radius of the meniscus at the flow split
s arc length
S speed ratio (U_2/U_1)
$\mathbf{t}$ a unit vector tangent to the free surface
$\mathbf{u}$ velocity vector, m/s
U speed, m/s
U_1 speed of the bottom roll, m/s
U_2 speed of the top roll, m/s
V_{gap} the vertical gap between the top and the bottom roll
x_0 x-coordinate of the attachment point
x_s x-coordinate for the flow split point
y_0 y-coordinate of the attachment point
y_s y-coordinate for the flow split point

Greek symbols

α pseudo time step, s
β slip coefficient
μ fluid viscosity, Pa s
ω relaxation factor
ρ fluid density, kg/m^3
θ_c contact angle
σ surface tension, $N\,m^{-1}$
δ identity tensor
$\boldsymbol{\tau}$ stress tensor
Ψ convergence factor
ξ unit displacement vector for the free surface

ACKNOWLEDGEMENTS

NSERC and Paprican provided financial support for this work. Prof. R. Marchand of Physics department, University of Alberta provided useful discussion on mesh generation and the mesh generator used in this work.

REFERENCES

1. Greener J, Middleman S. A theory of roll coating of viscous and viscoelastic fluids. *Polymer Engineering Science* 1975; **15**(1):1–10.
2. Savage MD. Mathematical models for coating processes. *Journal of Fluid Mechanics* 1982; **117**:443–455.
3. Savage MD. Mathematical model for the onset of ribbing. *AICHE Journal* 1984; **30**:999–1004.
4. Coyle DJ, Macosco CW, Scriven LE. Film-splitting flows in forward roll coating. *Journal of Fluid Mechanics* 1986; **171**:183–207.
5. Carvalho MS, Scriven LE. Capillary and viscoelastic effects on elastohydrodynamic lubrication flow film splitting in roller nips. *1994 International Printing and Graphic Arts Conference*, 1994; 259–266.
6. Carvalho MS. Roll coating flows in rigid and deformable gaps. *Ph.D. Thesis*, University of Minnesota, Minneapolis, Minnesota, 1997.
7. Carvalho MS, Scriven LE. Multiple states of a viscous free surface flow: transition from premetered to a metering inflow. *International Journal for Numerical Methods in Fluids* 1997; **24**:813–831.
8. Benkreira H, Edwards MF, Wilkinson WL. Roll coating of purely viscous liquids. *Chemical Engineering Science* 1981; **36**:429–434.
9. Wicks PJ, Decré M, Planguart Ph, Buchlin JM. Flow topology associated with disjoint eddies in an asymmetric film-splitting problem. *Physical Review E* 1995; **52**(2):R1281–R1284.
10. Decré M, Gailly E, Buchlin JM. Meniscus shape experiments in forward roll coating. *Physics of Fluids* 1995; **7**(3):458–467.
11. Schneider GB. Analysis of forces causing flow in roll coaters. *Transactions of the Society of Rheology* 1962; **6**:209–225.
12. Greener J, Middleman S. Theoretical and experimental studies of the fluid dynamics of a two-roll coater. *Industrial and Engineering Chemistry Fundamentals* 1979; **15**(1):1–10.
13. Coyle DJ, Macosco CW, Scriven LE. Stability of symmetric film-splitting between counter-rotating cylinder. *Journal of Fluid Mechanics* 1990; **216**:434–458.
14. Savage MD. Cavitation in lubrication: on boundary conditions and cavity fluid interfaces. *Journal of Fluid Mechanics* 1977; **80**:743–757.
15. Hopkins MR. Viscous flow between rotating cylinders and a sheet between them. *British Journal of Applied Physics* 1957; **8**:442–452.
16. Gaskell PH, Savage MD, Thompson HM. Stagnation-saddle points and flow patterns in Stokes flow between contra-rotating cylinders. *Journal of Fluid Mechanics* 1998; **370**:221–247.
17. Coyne JC, Elrod HG. Conditions for the rupture of a lubricating film. Part I theoretical model. *Journal of Lubrication Technology* 1970; **92**:451–456.
18. Fall C. A theoretical model of striated film rupture applied to the cylinder-plane. *Journal of Tribology* 1985; **107**:419–427.
19. Kubota T, Scriven LE. Forward roll coating in the runback feed condition. *Proceedings of the IS&T Coating Conference*, Boston, U.S.A., 1993; 309–318.
20. Deryagin BM, Levi SM. *Film Coating Theory*. Focal Press Ltd.: New York, 1959.
21. Kistler SF, Scriven LE. Coating flows. In *Computational Analysis of Polymer Processing*, Pearson JRA, Richardson SM (eds). Applied Science Publishers: New York, 1983; 243–299.
22. Sackinger PA, Schunk PR, Rao RR. A Newton-Raphson pseudo-solid domain mapping technique for free and moving boundary problems: a finite element implementation. *Journal of Computational Physics* 1996; **125**: 83–103.
23. Nickell RE, Tanner RI, Caswell B. The solution of viscous incompressible flows using finite element methods. *Journal of Fluid Mechanics* 1974; **65**(1):189–206.
24. Brezzi FF, Fortin M. *Mixed and Hybrid Finite Element Methods*. Springer: Berlin, 1991.
25. Marchand R, Carbounneau-Lefort M, Dumberry M, Provonost B. ARANEA, a program for generating unstructured triangular meshes with a Java graphical user interface, CPC Program Library, Queen's University of Belfast, N. Ireland, 2000.
26. Ruschak KJ. Boundary conditions at liquid-air interface in lubrication flow. *Journal of Fluid Mechanics* 1982; **119**:107–120.
27. Shikhmurzaev YD. Dynamic contact angles and flow in the vicinity of a moving contact line. *AICHE Journal* 1996; **42**(3):601–611.

28. Dussan VEB. On the spreading of liquids on solid surfaces: static and dynamic contact lines. *Journal of Non-Newtonian Fluid Mechanics* 1979; **11**:371–400.
29. Chen S, Higgins BG. Study of the flow in the upstream bank of liquid in a forward roll coater by the finite element method. *Chemical Engineering Science* 1988; **43**(10):2867–2875.
30. Huh C, Scriven LE. Hydrodynamic model of steady movement of a solid/liquid/fluid contact line. *Journal of Colloid and Interface Science* 1971; **35**(1):85–101.
31. Papanastasiou T, Malamataris N, Ellwood K. A new outflow boundary condition. *International Journal of Numerical Methods in Fluids* 1992; **14**:587–608.
32. Crouzeix M, Raviart PA. Conforming and non-conforming finite element methods for solving the stationary stokes equations. *RAIRO Analyse Numérique* 1973; **7**:33–76.
33. Silliman WJ, Scriven LE. Separating flow near a static contact line: slip at a wall and shape of a free surface. *Journal of Computational Physics* 1980; **34**:287–295.
34. Reglat O, Labrie R, Tanguy PA. A new free surface model for the dip coating process. *Journal of Computational Physics* 1993; **109**(2):238–246.
35. Hayes RE, Bertrand FH, Tanguy PA. Modeling of fluid/paper interaction in the application nip of a film coater. *Transport in Porous Media* 2000; **1441**:1–18.
36. Gaskell PH, Innes GE, Savage MD. An experimental investigation of meniscus roll coating. *Journal of Fluid Mechanics* 1998; **355**:17–44.
37. Young AE. A theoretical and experimental investigation of deformable roll coating. *Ph.D. Thesis*, University of Leeds, U.K., 1997.

